Title

Rationalizing Calcium Electrodeposition Behavior by Quantifying Ethereal Solvation Effects on Ca2+ Coordination in Well-Dissociated Electrolytes

Journal

Journal of The Electrochemical Society, 167(16)

ISSN

0013-4651

Authors

Driscoll, Darren M
Dandu, Naveen K
Hahn, Nathan T
et al.

Publication Date

2020-12-01

DOI

10.1149/1945-7111/abc8e3

Peer reviewed

Rationalizing Calcium Electrodeposition Behavior by Quantifying Ethereal Solvation Effects on Ca^{2+} Coordination in Well-Dissociated Electrolytes

Darren M. Driscoll,[a,b *] Naveen K. Dandu,[a,c] Nathan T. Hahn,[a,d] Trevor J. Seguin,[a,e] Kristin A. Persson,[a,e,f] Kevin R. Zavadil,[a,d] Larry A. Curtiss,[a,c] Mahalingam Balasubramanian[a,b *]

[a]Joint Center for Energy Storage Research, Lemont, IL, 60439

[b]Advanced Photon Source, Argonne National Laboratory, Lemont, IL, 60439

[c]Materials Science Division, Argonne National Laboratory, Lemont, IL, 60439

[d]Material, Physical and Chemical Sciences Center, Sandia National Laboratories, Albuquerque, NM 87185

[e]Energy Technologies Division, Lawrence Berkeley National Laboratory, Berkeley, CA 94720

[f]Department of Materials Science, University of California, Berkeley, CA 94720

[*]email: ddriscoll@anl.gov (D.M.D); mali@aps.anl.gov (M.B)

Abstract

Ca-ion electrochemical systems have been pushed to the forefront of recent multivalent energy storage advances due to their use of earth-abundant redox materials and their high theoretical specific capacities in relation to monovalent or even other more widely explored multivalent-charge carriers. However, significant pitfalls in metal plating and stripping arise from electrolyte decomposition and can be related to the coordination environment around Ca^{2+} with both the negatively charged anion and the organic–aprotic solvent. In this study we apply multiple spectroscopic techniques in conjunction with density functional theory to evaluate the coordination environment of Ca^{2+} across a class of ethereal solvents. Through the combination of X-ray absorption fine structure and time-dependent density functional theory, descriptive measures of the local geometry, coordination, and electronic structure of Ca–ethereal complexes provide distinct structural trends depending on the extent of the Ca^{2+}–solvent interaction. Finally, we correlate these findings with electrochemical measurements of $CaBHFIP_2$ salts dissolved within

this class of solvents to provide insight into the preferred structural configuration of Ca^{2+} electrolytic solutions for optimized electrochemical plating and stripping.

1. Introduction

Multivalent, metal-ion (M^{2+} = Ca^{2+}, Mg^{2+} or Zn^{2+}) chemistries have recently been on the forefront of next-generation battery materials as they can deliver a two-fold increase in charge capacity relative to analogous monovalent ion systems.[1] Additionally, a M^{2+} ion having a low reduction potential (-2.36 V for Mg & -2.87 V for Ca vs. SHE) allows for high cell voltage when the metal itself is used as the anode. However, the scientific progress of Ca^{2+} electrochemistry has lagged behind other dicationic species in recent years in part because of the need for aprotic solvents with high reductive stability in order to mitigate parasitic reactions at the metal anode during electron transfer processes.[2-5] Specifically, a class of ethereal solvents has been shown experimentally as a promising medium for transferring Ca^{2+} ions to electrode surfaces within the electrolytic matrix mainly due to their significant reductive stability.

Currently, only a few calcium salts have been successful in reversible plating and stripping at room temperature on an electrified surface including: $Ca(BH_4)_2$ and calcium tetrakis(hexafluoroisopropoxy) borate ($CaBHFIP_2$) dissolved within ethereal solvents.[6-9] While these systems produce semi-reversible Ca^{2+} electrochemistry, both have major drawbacks limiting their overall use in electrochemical systems. The $Ca(BH_4)_2$ system suffers from instability of the BH_4^- anion in oxidative environments and is therefore limited to roughly 3 V vs. Ca/Ca^{2+}.[6] On the other hand, BHFIP provides a larger electrochemical window (~ 4 V) and the potential for greater cell voltage. In reference to the specific electrolyte compositions, the pioneering work focused on $CaBHFIP_2$ dissolved in the linear ethereal solvent, 1,2-dimethoxyethane (DME or G1).[7, 8] More

recently, longer chain ethereal compounds such as diglyme (DGM or G2) and cyclic ethers, such as tetrahydrofuran (THF), have been shown to promote either improved or comparable Ca electrodeposition reversibility in relation to the nascent electrolyte system.[9] However, similar measurements using triglyme (G3), a longer linear ethereal solvent, provided negligible success.[10] While many of these electrolyte compositions provide promising steps towards reversible Ca^{2+} electrochemistry, each exhibits susceptibility to decomposition leading to the formation CaF_2 layers and organic byproducts on the electrode surface that inhibit calcium diffusion.[8-10] For example, a comparison of the compositions of calcium deposits by energy dispersive X-ray analysis revealed that using THF as the supporting solvent leads to greater relative F content while using G1 or G2 leads to greater relative O content.[9] These differences suggest that the solvent and specifically the local coordination around the cationic species plays an equally important role in the reversibility of the calcium deposition process.

Only a few studies have attempted to quantify the rich solvation environment within these Ca^{2+} aprotic systems.[11-13] Lapidus et al. evaluated the coordination environment of $CaTFSI_2$ [TFSI = bis(trifluoromethanesulfonyl)-imide] salts in diglyme using X-ray pair distribution function combined with molecular dynamics (MD) simulations and identified noticeable contact ion-pair behavior in the bulk electrolyte.[11] In fact, the large ionic radius of 1.00 Å for Ca^{2+} has been suggested as a major factor for ligand attachment that can range from traditional 6-fold coordination all the way up to 8 or 9 attachments depending on the size and configuration of the ligand.[14, 15] As a result, the large size of Ca^{2+} can act to drive anionic association within the electrolytic solution, which can inhibit rapid transport of ions or induce anion reduction at the electrode surface.[10, 16, 17] In fact, our most recent work combined spectroscopic analysis with MD simulations to characterize ion association tendencies in ethereal-$CaTFSI_2$ electrolytes in which

we found the solvent:Ca^{2+} coordination strength to increase as 2-MeTHF < THF < G1 < G2 < G3 with clear evidence of Ca^{2+}–TFSI contact ion-pairs even with G2 solvation.[10] These factors all reveal the critical importance of the Ca^{2+} solvation environment for electrochemical deposition and stripping of Ca metal.

In order to develop a full understanding of the Ca^{2+} coordination tendencies during solvation, a selective probe of the Ca environment must be included in the overall electrolyte analysis. An excellent example is the utilization of Ca K-edge X-ray absorption spectroscopy (XAS) to understand local coordination and electronic structure.[15, 18-21] Analyses of the X-ray absorption near edge spectroscopy (XANES) and extended X-ray absorption fine structure (EXAFS) have been combined with a variety of theoretical methodologies to study the local electronic structure and structural geometries of both non-aqueous and aqueous Ca^{2+} environments.[15, 18-23] Previously, we have characterized the solvation environment of $Ca(BH_4)_2$ dissolved within THF complexes through the combination of XAS and vibrational spectroscopy.[13] Through identification and quantification of small but clear changes in the EXAFS we were able to describe the presence of both Ca-BH_4 contact ion pairs and Ca-Ca dimer species—both of which play crucial roles in the presentation of available Ca^{2+} to the electrode surface for metal deposition.[13] However, the BHFIP anion is considered "weakly associating" as suggested by a highly delocalized electronic structure,[24] single crystal XRD data[8] and recent comparisons between solvation structures of BHFIP and TFSI in identical ethereal solvents.[10] All of these recent findings suggest that the Ca^{2+}-solvent interaction plays an equally critical role in these electrochemical processes by determining the extent of anion coordination and the structure and dynamics of the electrochemically active species.

In this study we combine vibrational and X-ray absorption spectroscopies with density functional theory (DFT), time-dependent DFT (TDDFT) to provide a comprehensive analysis of the structural and electronic trends of Ca^{2+} solvation within a class of ethereal solvents. We show through both measured and computed Raman investigations that Mg^{2+} and Ca^{2+} salts of the bulky fluorinated alkoxyborate anion, BHFIP, dissociate readily in ethereal–solvent systems at moderate concentrations. Through careful analysis of the XANES and EXAFS regions of the XAS spectra, we can identify trends in solvent chelation that relate these to the binding symmetries and configurations around the Ca^{2+} atom. These results allow us to interpret recent analyses of Ca-ion electrochemistry and draw clear relationships between the solvation structure of Ca^{2+}–ethereal complexes and the performance of these complexes in electrochemical applications.

2. Experimental / Methods

Electrolyte Synthesis. All reagents were purchased from Millipore-Sigma. Solvents were distilled and stored over activated alumina and molecular sieves before use and possessed water content < 10 ppm. The $CaBHFIP_2$ salt was synthesized by reacting $Ca(BH_4)_2$ with dry hexafluoroisopropanol (99.9%) in THF or G1, in a manner similar to previous reports.[7, 9] After removing the solvent under vacuum, the salt was recrystallized using dry hexane. Final vacuum treatment at room temperature yielded solvate salts with approximate formulas of $CaBHFIP_2$*$THF_{1.5}$ and $CaBHFIP_2$*$G1_2$ based on ^{1}H NMR (supporting information, Fig. SI.1). The THF solvate was used to prepare THF-based electrolytes for spectroscopic analysis to avoid interference from any residual G1 in solution. The G1 solvate was used to prepare electrolytes for spectroscopic analysis in distilled G1, G2, and G3; the latter two electrolytes were treated under vacuum to remove the residual G1. Salts of $MgBHFIP_2$ used for Raman analysis were synthesized in an analogous fashion using $Mg(BH_4)_2$ as a starting material.

Electrochemical. Voltammetric electrochemical testing was performed in three-electrode cells using polished Au working electrodes (0.02 cm^2) and calcium rod reference and counter electrodes that were abraded to produce a fresh metal surface before use. Cyclic voltammetry was performed using a Solartron Modulab potentiostat. In order to minimize the influence of impurities or synthetic byproducts, the electrolytes used in these experiments were generated by dissolving a $CaBHFIP_2$*$G1_2$ solvate (0.2 M) into distilled THF, G1, or G2.

2.1 Ca^{2+} Solvation Characterization

Raman Spectroscopy and NMR. Raman spectroscopy was performed on a Witec Confocal Raman Microscope equipped with a 532 nm laser and calibrated using the silicon peak at 520.4 cm^{-1}. The frequency resolution is ~0.7 cm^{-1} across the measured region of interest. Samples were measured in sealed glass vials at room temperature. ^{1}H NMR was performed on a Bruker Avance 500 MHz instrument.

XAS. X-ray absorption spectroscopy was performed at the Ca K-edge using beamline 9-BM of the Advanced Photon Source. Liquid electrolytes were dispersed onto porous polyolefin discs (Celgard), sealed within an aluminized-mylar pouch and positioned at a 45° angle relative to the incident beam. A Si(111) monochromator and a Rh coated mirror for harmonic suppression with a cutoff energy of 6 keV were both used. Measurements of the 0.2 M samples were acquired in fluorescence mode using an ionization gas chamber before the sample (20 % N_2, 80% He) and an energy dispersive, multi-element fluorescence detector (Vortex-ME4). Based on the concentration regime used within the experiments, self-absorption effects were expected to be minimal. The data were dead-time corrected to account for saturation effects of the fluorescence detector, and the total count rate did not exceed 80000 counts per second for each element at the Ca white line.

The energy scale of the XAS data was calibrated by defining the first derivative maximum of a titanium foil absorption spectra as 4966 eV. Energy reproducibility was checked by periodically measuring the spectra of the Ti foil. XAS data were normalized to unit step height as previously described[13] using the Athena software package.[25] X-ray absorption pre-edge structure was analyzed using XASViewer within Larch.[26] Pre-edge features were edge-subtracted using the combination of a Lorentzian to define the absorption edge and a linear function for the pre-edge background with the pre-edge peaks fit to Voigt functions.

Ejected photoelectrons are defined by their wavenumber (*k)* in relation the absorption edge energy (E_0) through the equation:

$$k = \sqrt{2m_e(E - E_0)/\hbar^2} \qquad (1)$$

The experimental EXAFS oscillations of each sample, χ(k), are extracted from the normalized XAS data using subtraction of a spline and a cutoff distance (R_{bkg}) of 1.3 Å. In the Ca K-edge EXAFS, three multi-electron transitions appear at roughly 2.7, 3.1 and 10.3 $Å^{-1}$.[15, 20] The multi-electron excitation (MEE) at 10.3 $Å^{-1}$ was accounted for using an arctangent correction function. For analysis of the EXAFS region, we use the EXAFS relationship given by:

$$\chi(k) = \sum_i \frac{F_i(k) S_0^2 N_i}{kR_i^2} e^{-2k^2\sigma_i^2} e^{\frac{-2R_i}{\lambda(k)}} \sin\left(2kR_i + \delta_i(k) - \frac{4}{3}k^3 C_{3,i}\right) \qquad (2)$$

where the index, *i,* is considered the path index and the χ(k) is calculated as the summation over all paths.[27] Theoretical standards for each Ca^{2+}-solvent photoelectron scattering path were generated by the *ab initio* code, FEFF6,[28] using MD-optimized geometries of solvent configurations around Ca^{2+} atoms as a starting point.[10] In eq. 2, $F_i(k)$, $\delta_i(k)$, and $\lambda(k)$ represent the effective scattering amplitude, total phase shift, and mean-free-path of the photoelectron and each

are derived from the aforementioned code, FEFF6. The many-body amplitude-reduction factor, S_0^2, is fixed to 0.95 as previously described in literature and consistent with previously studies of Ca^{2+} in oxygen-coordinating aprotic systems.[13, 15] Therefore, the parameters still to be fit include, N_i, the degeneracy of the path (and therefore the coordination number for single scattering paths), R_i, the half-path length, σ^2_i, the Debye-Waller factor and $C_{3,i}$, the asymmetry of the distribution. Variation of $C_{3,i}$ was found to provide negligible improvements on the single scattering paths and thus not included in the fitting process. Additionally, a single nonstructural parameter for all paths, ΔE_0, is varied to align the k=0 point of the experimental data and theory. Fitting of the experimental data to the standards was employed using the Artemis software package using the experimental χ(k) data weighted by $k^1 - k^3$.[25] Full details of the photoelectron scattering paths used in glyme-based Ca^{2+} solutions have been described previously[10] and specific path contributions including assumptions used to limit the number of independent variables are provided in the SI.

2.2 Computational Studies

*Geometry Optimization for XAS studies***.** Computational studies were performed for the geometries that contain Ca^{2+} at 6, 7 and 8-fold coordination with two different ethereal solvents, THF and G1. Counter anions were not included in their geometries. Optimization of all geometries were done under unrestricted Kohn-Sham density functional theory (DFT) method using the TPSS functional[29] and the Def2-TZVP basis set[30] in association with Def2-TZVP/J auxiliary basis set[31] implemented in the ORCA4.2.0 code.[32] Grid5 (Lebedev434) was used as a DFT integration grid for reliable geometry optimizations and final energies. The obtained optimized geometries are then used for computing their K-edge pre-edge spectra. The computed bond distances (Table SI.1) between Ca and 'O' of solvent are consistent with the experimental values.

Simulations of XAS Measurements. The XAS spectra were computed using Time-Dependent DFT (TDDFT) approach as employed in ORCA4.2.0 code, performed at RIJCOSX[33] approximation. For this approach, we used BHLYP functional as it was found to provide appropriate assignments of relative pre-edge energies, closer to the experimental values.[18] The same basis set and grid as implemented in the TPSS optimization steps were used. In these calculations we invoke quadrupole interactions, essential for determining pre-edge peaks, using the DoQuad key word. A total of 40 transitions was requested. Spectra were calculated using a broadening of 1.2 eV and their energy shifted by 50.4 eV to align with experimental pre-edge region.

Simulations of Raman Spectroscopy. Computed Raman spectrum data were obtained from optimized geometries using Gaussian16[34] at the wB97X-D/6-31+G(d) level of theory.[35] Geometries were verified as minima by the absence of imaginary frequencies.

3. Results and Discussion

In this study, a combination of spectroscopic techniques and density functional theory have been performed to quantify the impact of solvent coordination around Ca^{2+}. X-ray absorption measurements of the Ca K-edge provide a quantitative, element specific analysis to the bulk solvation structure. The measurements described herein, combined with time-dependent density functional theory calculations, depict a clear understanding of Ca^{2+} coordination structures and geometries that play a crucial role in electrochemical Ca^{2+} deposition and Ca^{0} stripping.

3.1. Spectroscopic Characterization of Ca^{2+} $BHFIP^{-}$ Solvation Structures

Alkaline earth (M = Mg^{2+} or Ca^{2+}) salts of the BHFIP anion are thought to readily dissociate or at most exhibit weak interactions in a variety of ethereal solutions based on their

extremely high ionic conductivities.[7, 8, 10, 36] As shown with many electrolyte systems within organic solvents, the vibrational motions of anion and solvent can provide clear evidence of the extent of association between cationic and anionic species in solution.[37] As shown in Figure 1, we employed Raman spectroscopy to identify the extent of dissociation in a variety of ethereal solvents (THF, G1, G3) based on comparison with the corresponding partially de-solvated salt spectra (either $CaBHFIP_2*THF_{1.5}$ or $MgBHFIP_2*THF_1$). Each sample spectrum exhibited a sharp vibrational feature at ~720 cm^{-1} that is distinct from any solvent bands and is attributed to the ν(C-F) mode of BHFIP based on DFT calculations of the free anion and idealized contact-ion pair shown in Figure 1c (comparison of the ν(B-O) region can be found in Fig. SI.2). These calculations predict that dissociation of the metal-BHFIP ion pair should result in a blue-shift of the ν(C-F) frequency. Indeed, all measured solution spectra (whether containing Ca^{2+} or Mg^{2+}) yielded a nearly equivalent ν(C-F) band and exhibited a blue-shift in frequency relative to the corresponding salt containing ion association (Fig. 1a-b). While the extent of blueshift for the salt-solutions is not as significant as suggested by the idealized DFT structures, the equivalence of these blue-shifted ν(C-F) frequencies regardless of solvent indicates a consistent BHFIP environment, which is most logically identified as non-coordinating. The fact that facile dissociation of the salt occurs in all these solvents even at near saturated concentrations of ~0.5 M argues that Ca^{2+} and Mg^{2+} cations are preferentially coordinated by these ethereal solvents and are therefore minimally impacted by direct BHFIP coordination in solution. That this occurs despite significant variation in coordination strength of these solvents highlights the especially weak coordinating character of BHFIP.[10] Therefore, the first solvation shell of the metal cation is defined entirely by the solvent molecules. However, the vibrational spectroscopic measurements depicted do not provide detailed

information concerning cation-solvent coordination, which is a critical factor controlling the overall solvation structure, transport, and stability for the Ca^{2+}–electrolytic systems.

XAS measurements of Ca^{2+} ions solvated by the ethereal solvents were performed to understand the local coordination and physical properties of solvation arising from solvent chelation. The BHFIP anion, as verified through Raman spectroscopy, readily dissociates from Ca^{2+} in contrast to other anions such as BH_4^- and $TFSI^-$ within aprotic solutions.[11-13] Therefore, $CaBHFIP_2$ salt solutions of 0.2 M provide a concentration regime with high ion conductivity in which we expect the majority of the Ca^{2+} ions to be fully solvated and the BHFIP to exist in a free or solvent separated ion-pair (SSIP) state—providing a solution environment where Ca^{2+}-solvent local environments dominate.[10, 12] As illustrated in Figure 2, the Ca^{2+} coordination environment exhibits significant differences in X-ray absorption spectrum depending on the solvent at the pre edge region (4040 - 4042 eV), the absorption edge (~4044.5 eV) and above the absorption edge. These differences spectral intensity and line-shape can be attributed to changes in the coordination geometry and spatial position of coordinating atoms across the ethereal solvent series. While the overall goal of x-ray absorption measurements will be to identify fine differences in every portion of the XAS spectrum of solution-phase speciation, the scope of this manuscript will focus specifically on understanding differences in the pre-edge and the EXAFS oscillations.

3.2. Sensitivity of the XANES to Coordination Geometry: Pre-edge Simulations

Closer inspection of the pre-edge region within the XANES provide clear indication of a unique structural geometry for the $CaBHFIP_2$/THF solution. After performing a background and absorption edge subtraction, the pre-edge spectra (Fig. 2b) depict a clear double pre-edge feature only when Ca^{2+} is coordinated to THF (Fig. 2b, red trace). Conversely, the pre-edge of Ca^{2+} bound to the any of the studied glyme solvents reveals only a single broad feature. The pre-edge shape of

Ca K-edge XAS measurements has previously been ascribed to 1s to 3d transitions and increases in intensity with decreasing symmetry around the absorber.[15] Two specific components, quadrupolar coupling and p orbital character mixing with the d states are important, with the latter contributing to more intense transitions. The two-peak pre-edge split by roughly ~1.1 eV, present for only the Ca-THF system (see spectral fitting in Fig. SI.3), suggests 6-fold coordination.[18] The single broad pre-edge feature found with Ca–glyme systems is likely an indication of increased coordination (between 7-9) and an average of multiple coordination environments with multidentate interactions between an ethereal solvent molecule and Ca^{2+} as recently suggested by ab initio MD with metadynamics sampling.[10] To systematically explore THF solvation of Ca^{2+}, we initially performed TDDFT calculations on two different cationic systems (1) a pseudo-octahedral geometry of Ca^{2+} coordinated with six THF molecules, and (2) a Ca^{2+} coordinated with seven THF molecules. The simulated spectra of these $Ca(THF)_n^{2+}$ complexes, as illustrated in Figure 3, depict noticeable differences in both pre-edge intensity and spectral line-shape as a function of structural configuration. Specifically, the $Ca(THF)_6^{2+}$ complex is shown to have a split pre-edge with the two features separated by roughly ~1.1 eV. A comparison between the experimental XANES pre-edge of the $CaBHFIP_2$/THF electrolyte and the theoretically derived pre-edge spectra suggests that Ca^{2+} prefers a six-coordinated octahedral structure in THF (Fig. 3a, red trace). While the dominant presence of the six-coordinated Ca^{2+} complex is now elucidated, we note there are some differences in the intensity of the relative peak heights between theory and experiment. Theory uses a single, well defined structure (Table 1), but in "real" solutions there is likely significant disorder both from thermal and static effects. Additional calculations have been performed to understand the effect of disorder on the pre-edge intensity within an overall octahedral complex and are discussed later.

The two $Ca(THF)_n^{2+}$ complex configurations simulated by the TDDFT methods yield significant differences in peak intensities and line-shapes for the pre-edge region (Fig. 3). The electronic origins of intensity at the Ca pre-edge can be described as either dipole allowed (1s → *n*p + 3d) or quadrupole (1s → 3d) transitions into unoccupied electronic states. Each simulated structure contains components of both types of transitions in the pre edge and these are tabulated in the Table 1. Differences between dipole and quadrupole components within the pre edge provide clear explanations of the intensity differences observed between the two structures. As shown in Table 1, in the case of $Ca(THF)_6^{2+}$, due to the presence of a center of symmetry, there is less dipole transition intensity, resulting in a contribution primarily from quadrupole transitions and a low total absorption intensity (roughly an order of magnitude lower than $Ca(THF)_7^{2+}$) in the pre-edge region. However, in case of $Ca(THF)_7^{2+}$, due to the absence of the center of inversion symmetry, mixing of p states and d states becomes favorable, the dipole transition predominates and results in an increase in overall intensity of the pre-edge.

The significant difference in pre-edge intensity between the two structures can be fully explained by the lack of dipole transition in the $Ca(THF)_6^{2+}$ complex; however, it does not entirely explain the pre-edge double peak structure with a ~1.1 eV separation. To understand the nature of the double peak, we have investigated difference density maps of the individual molecular orbitals that are contributing to the pre-edge region (Fig. 4). Due to stronger interactions between e_g orbitals and the ligands, in comparison to t_{2g} orbitals, the e_g orbitals are slightly destabilized and shift to higher energy. Thus, we observe a double peak pre-edge for the case of $Ca(THF)_6^{2+}$ due to the increased energy splitting of the d-orbitals. The Ca^{2+} within the $CaBHFIP_2$/THF electrolyte must therefore contain a majority 6-fold coordination structure, otherwise the pronounced double pre-edge feature would become a single broad feature as suggested by the TDDFT calculations of the

$Ca(THF)_7^{2+}$ complex. In fact, we can experimentally account for the change from the pronounced double pre-edge feature, shown in the $Ca–THF_6$ complex, to a broader, less resolved single feature by including a strongly associating anion, such as TFSI. Ca^{2+}–TFSI interactions produce contact ion pairs (in addition to partial THF solvation)[10] and thereby perturb the local electronic structure upon ion-association by forming a non-symmetric Ca-O coordination sphere (Fig. SI.4). XANES measurements coupled with TDDFT calculations clearly identify that the local symmetry of the Ca/THF complex is dominantly of octahedral symmetry.

Due to the inherent solvent exchange dynamics present in solution, we would expect a variety of Ca – O bond lengths to exist across an ensemble average of Ca^{2+}-complexes. Indeed, based on our EXAFS data, the Ca-O bond distances in these ethereal solutions contain structural disorder on the order ~0.1 Å as described by Debye Waller factors for these bonds (see below for EXAFS analysis). In order to computationally simulate this structural disorder, we systematically altered the distance of one of the axial Ca-O bond from its original optimized value at 2.43 Å in the pseudo octahedral $Ca(THF)_6^{2+}$ structure. We observed that by varying a single axial bond distance the resulting spectrum of the pre-edge is clearly altered. With an increase in bond distance, we observed that the intensities and degree of splitting of the d- orbitals are affected. As shown in Figure 5, increasing the Ca-O bond distance progressively merges the two pre-edge peaks due to loss of symmetry while decreasing the Ca-O bond distance more strongly differentiates these two peaks as transitions to the e_g and t_{2g} orbitals become more separated in energy.

Similarly, TDDFT calculations of the $Ca(G1)_n^{2+}$ complexes were performed for three different Ca-O coordination numbers (6, 7 and 8), and their optimized structures are shown in Figure SI.5. The computed Ca K-edge XANES pre-edges for each structure, along with the experimental spectra, are shown in Figure 6. Additionally, similar calculations were performed for

$Ca(G1)_4^{2+}$ having 2 monodentate ligands at the axial positions and 2 bidentate ligands at equatorial positions to generate a symmetric octahedral environment (Fig. 6, green trace). In this fully symmetric octahedral geometry, the intensities were reduced about 10 times compared to the fully bidentate, distorted octahedral 6-fold geometry of $Ca(G1)_3^{2+}$ (fig 6, red), indicating that a fully symmetric octahedral structure decreases the overall intensity of the pre-edge significantly. Similar to the calculated spectra of $Ca(THF)_6^{2+}$, simulated 6-coordinated G1 structures with low-to-moderate distortion, exhibit a double peaked pre-edge feature. However, in the $CaBHFIP_2$/G1 solution, such a feature is not found experimentally and is therefore not a prevalent species in solution. Based on the relative intensity of the simulated pre-edge feature (simulated spectra are not multiplied to match experimental data in Fig. 6), the primary calcium species in the solution are likely from a variety of structures: $Ca(G1)_4^{2+}$ complexes with 7 or 8 Ca-O bonds. However, based on the studies presented, we cannot rule out minority complexes that include distorted or pristine octahedral species within the ensemble averaged solvation environment.

3.3 Defining Coordination Structures Through EXAFS Modeling.

Analysis of the XANES pre-edge through both experimental and TDDFT measurement describes the coordination symmetry and electronic structure around the Ca atom. However, the EXAFS oscillations —at energies above the absorption edge—provide direct insight into local structure around the Ca^{2+} ion. EXAFS measurements of the Ca^{2+} environment as a function of ethereal solvent are provided in Figure 7. Upon Fourier transform of the $\chi(k)$, we can identify noticeable photoelectron contributions in the EXAFS to at least 4 Å (in non-phase corrected plots, Fig. 7b-c) and therefore provide analysis of first shell interactions (such as the Ca-O interactions mentioned previously) as well as Ca–C interactions, also originating from the solvent molecules (schematic representation of photoelectron paths shown in Fig. SI.6). Noticeable differences

between glyme-solvated systems and THF-solvated systems can be identified in both k-space (by looking at the change in oscillation phase over the full $Å^{-1}$ range in Fig. 7a) and in r-space, which clearly show drastic changes in the second shell structure (2.2 – 3.2 Å in Fig. 7b-c). We expect THF solvation to behave differently compared to glyme solvation because the linear, flexible glyme structure can conceivably form bidentate, tridentate or tetradentate interactions with a single Ca^{2+}, depending on the chain length. Whereas, the THF–Ca interaction is localized to a single oxygen atom on the cyclic ether and produces an EXAFS signal with noticeably weaker Ca–C correlations that are likely caused by an increase in vibrational and rotational freedom of the ligand, a decrease in Ca-C degeneracy due to the weaker coordination sphere or a combination of these factors resulting in an overall less prominent second shell contribution. The proposed weaker coordination of the THF ligand is seemingly at odds with the shorter Ca–O bond distance found experimentally in the THF system (see r-space plots of each solvent, Fig 7B-C). However, the Ca^{2+} effective ionic radius is dramatically altered by the number of coordinating ligands and has been shown to increase by ~0.06 Å per unit increase in coordination.[38] We suggest that the measured decrease in Ca–O bond length for THF coordinating systems (compared to glyme coordination) is therefore related to the effective ionic radius of the Ca^{2+} when only bound to an octahedral of coordinating THF molecules. Still, the total solvation of Ca^{2+} with THF is likely energetically weaker compared to glyme solvation as evidenced by the weaker second shell contribution in the EXAFS of THF solvating systems. With regard to the glyme series, a noticeable increase in the second radial feature, ~ 3 Å in Figure 7c, occurs from G1 to G3. Qualitatively, we hypothesize this change in magnitude to be a result of a more stabilized coordination of the glyme to Ca^{2+} as the longer glymes can form a larger number of multidentate bonds to the cation and thereby create a

more rigid structure. This is consistent with our recently reported Raman results, which argue for a solvent:Ca^{2+} coordination strength trend of G1 < G2 < G3.[10]

A more rigorous, quantitative assessment of the coordination environment around Ca^{2+} ions was performed through fitting the EXAFS experimental data to computational models of glyme coordination. Representative configurations generated through MD simulations, used previously to model $CaTFSI_2$/glyme systems, were used as initial inputs to generate individual photoelectron scattering paths using the FEFF6 code.[10, 28] Individual photoelectron scattering paths included the Ca–O, Ca–C and Ca–O–C multiple scattering paths and assumed a bidentate configuration (as shown in Fig. SI.6). The overall fits of the EXAFS data for $CaBHFIP_2$ dissolved within each glyme are provided in Figure 8. A table of important parameters used to fit the solvation systems of all three glymes is shown in Table 2; a full list of parameters can be found in Table SI.2. From the fitting parameters of the glyme systems shown in Table 2, we unequivocally identify the first main oscillation in the r-space data as the Ca–O contribution. Across all three solvents, this bond distance is relatively unchanged except for a slightly longer evaluated bond distance for the G1 coordination of ~0.03 Å.

Unfortunately, equivalent EXAFS fits of the $CaBHFIP_2$/THF system provided less convincing statistical results. Calcium–oxygen bond distances in THF can be fit to 2.40 ± 0.06 Å with a Ca–O coordination number of 6 ± 1. However, attempts to model the Ca–C scattering paths proved unsuccessful. We speculate the configuration of the THF molecules around each Ca^{2+} contain substantial vibrational and rotational freedom and therefore the resulting ensemble averaged photoelectron signal of those second shell atoms become diminished. Future studies plan to understand the phenomena, which has been identified across similar THF–based systems.[10] Nonetheless, analysis of both the EXAFS and XANES regions of the X-ray absorption spectrum

suggests a local structure dominated by an octahedral $Ca(THF)_6^{2+}$ species, which clearly depicts structural differences in coordination compared to the glyme series.

For the glyme series, calculated parameters from the three fits provide evidence of coordination and structural changes as a function of glyme length during the solvation of Ca^{2+}. We first note the increase in amplitude of the G3 coordinated Ca complex and postulate an overall ordered coordination environment for this Ca^{2+}–solvent complex. The data provided in Table 2 and Figure 8 suggests G3 coordination likely induces an increase in the number of Ca–O correlations relative to the smaller glymes (G1, G2) studied and provides consistent results with recent molecular dynamic simulations using metadynamics sampling for Ca solvation within the glyme series.[10] The average coordination of oxygen atoms to Ca^{2+} is shown to steadily increase as a function of the number of accessible oxygen atoms in the solvating linear ethereal molecules. While the EXAFS measurements cannot definitively quantify a combination of two nearly identical coordination environments, the overall trend in coordination number as a function of coordinating solvent suggests the larger effective ionic radius of Ca^{2+} species dictates a more flexible first shell environment compared to smaller, dicationic species such as Zn^{2+} or Mg^{2+} for which octahedral environments are typically preferred in solution.[11, 38-42] Additionally, the most notable difference in the calculated EXAFS fits between solvent systems is the disorder term associated with the Ca–C path (and Ca–O–C multiple scattering path) found roughly 3-4 Å away from the Ca^{2+} ion. As depicted in Figure 7c, the second oscillatory feature in r-space increases with coordination to larger glyme molecules. This is likely the product of a more ordered shell around the Ca^{2+} ion and is numerically depicted through the decrease in the Debye Waller factor of the photoelectron scattering paths attributed to the carbon atoms at ~3.5 Å away from the absorbing

atom. The increase in ordering of the carbon atoms around the Ca ion suggests a more rigid coordination as the glyme chain increases from G1 to G2 to G3.

3.4. **Relationship between Solvent Coordination and Electrochemical Performance.**

The aforementioned spectral and computational analysis of the four ethereal $CaBHFIP_2$ electrolytes demonstrates explicit relationships between solvent structure, preferred Ca-O coordination number, and structural disorder. These findings support a growing connection between solvent:Ca^{2+} coordination tendencies and overall efficiency for calcium electrodeposition and stripping, which is determined by the stability and dynamics of the interfacial complexes. $CaBHFIP_2$ electrolytes dissolved within THF, G1, and G2, have all demonstrated calcium deposition reversibility with columbic efficiency (CE) values ranging from 60 - 85% depending on the experimental conditions.[7-10] Our own electrochemical measurements are generally consistent with these observations as well (supporting information, Fig. SI.8). Whereas, our measurements of the same salt dissolved within G3 have shown only minimal—likely parasitic—reduction and a complete failure to provide reversible metallic stripping.[10] Interestingly, in comparing THF, G1, and G2, Nielson et al. found greatest relative fluorine content for calcium deposited in THF whereas calcium deposited in G1 and G2 contained significant oxygen and carbon impurities and a more modest amount of fluorine.[9] The decomposition products found are therefore suggestive of anion decomposition with the more weakly bound THF and solvent decomposition with the more strongly coordinating glymes. The unique coordination environment of the $CaBHFIP_2$/THF electrolyte, with its double pre-edge XANES feature indicative of 6-fold coordination geometry, could provide insight into the differences in chemistry at the electrode surface. Whereas all three solvents favor the formation of fully solvated Ca^{2+} in the bulk electrolyte, the lower coordination number preferred by THF may allow for greater anion

interactions in the vicinity of the electrode, either with the de-solvating Ca^{2+} cation, a partially reduced Ca^{+} cation, or with deposited Ca^{0}, all of which could potentially induce a greater extent of anion decomposition.

Overall, the columbic efficiency (CE) for reversible Ca^{2+} electrochemistry seems to reach a threshold upon solvation with G2. A solvent that provides strong, ordered chelation of Ca^{2+} (e.g. G3) shows limited reversibility compared to the weaker coordinating solvents. Combined with the analysis of the local electronic structure and coordination, depicted by the XANES and EXAFS data, we believe stronger chelating solvents, e.g. G3, inhibit desolvation. Concurrently, the desolvation penalty likely allows for a greater probability of adverse side reactions on the electrode surface—thereby inhibiting both plating and subsequent stripping processes over continuous cycling. Whereas, glymes of intermediate coordination strength (G1, G2) enable more efficient desolvation, plating and stripping processes with minimal anion decomposition.

4. Conclusion

In conclusion, we have used multiple spectroscopic techniques combined with computational modeling to study the solvation structure of Ca^{2+} within typical ethereal electrolyte solvents. Raman spectroscopy suggests the bulky, fluorinated alkoxyborate anion, BHFIP, dissociates from either Ca^{2+} or Mg^{2+} within a wide range of ether-based solvents. These solvents, ranging from the cyclic ethers like THF to long linear ethereal molecules like the glyme series exhibit remarkable differences in each of their local solvation structures around Ca^{2+} as evidenced by drastic changes in the Ca K-edge X-ray absorbance spectra of each solution. Through experimental and

computational analysis of the XANES pre-edge, we identify a unique double peak, pre-edge absorption profile that can be attributed to 6-fold octahedral structure for THF bound to Ca^{2+}. Whereas, glyme coordination, with multiple oxygen coordinating contact points on each molecule, is found to form a more rigid solvation structure with significantly higher numbers of Ca–O ligands as the length of the glyme (G1 to G3) increases. These solution-phase structural differences all play a critical role in the performance on Ca electrochemistry reversibility; weakly coordinating solvent (THF) may allow nearby anions to participate in the electron transfer process at the negative electrode whereas a too strongly chelating solvent (G3) inhibits desolvation of Ca^{2+} due to a rigid coordination structure. These findings suggest the solvation structure (both anion and solvent) around each Ca^{2+} is critical for understanding electrochemical performance and reversibility of specific electrolyte compositions.

Acknowledgements

This work was supported by the Joint Center for Energy Storage Research, an Energy Innovation Hub funded by the U.S. Department of Energy. This research used resources of the Advanced Photon Source, an Office of Science User Facility operated for the U.S. Department of Energy (DOE) Office of Science by Argonne National Laboratory and was supported by the U.S. DOE under Contract No. DE-AC02-06CH11357. Sandia National Laboratories is a multimission laboratory managed and operated by National Technology & Engineering Solutions of Sandia, LLC, a wholly owned subsidiary of Honeywell International Inc., for the U.S. Department of Energy's National Nuclear Security Administration under contract DE-NA0003525. This paper describes objective technical results and analysis. Any subjective views or opinions that might be expressed in the paper do not necessarily represent the views of the U.S. Department of Energy or

the United States Government. We thank Dr. George Sterbinsky for help with experiments at 9-BM.

ORCID

Darren M. Driscoll: 0000-0001-8859-8016
Naveen K. Dandu: 0000-0001-7122-8537
Nathan T. Hahn: 0000-0001-6187-4068
Kristin A. Persson: 0000-0003-2495-5509
Kevin R. Zavadil: 0000-0002-3791-424X
Larry A. Curtiss: 0000-0001-8855-8006
Mahalingam Balasubramanian: 0000-0002-3988-3125

References

1. J. Muldoon, C. B. Bucur, and T. Gregory, *Chem. Rev.*, **114** (23), 11683-11720 (2014).
2. A. Ponrouch, C. Frontera, F. Bardé, and M. R. Palacín, *Nat. Mater.*, **15** 169 (2015).
3. D. Aurbach, R. Skaletsky, and Y. Gofer, *J. Electrochem. Soc.*, **138** (12), 3536 (1991).
4. M. E. Arroyo-de Dompablo, A. Ponrouch, P. Johansson, and M. R. Palacín, *Chem. Rev.*, **120** (14), 6331-6357 (2020).
5. A. M. Melemed, A. Khurram, and B. M. Gallant, *Batteries & Supercaps*, **3** (7), 570-580 (2020).
6. D. Wang, X. Gao, Y. Chen, L. Jin, C. Kuss, and P. G. Bruce, *Nat. Mater.*, **17** 16 (2017).
7. Z. Li, O. Fuhr, M. Fichtner, and Z. Zhao-Karger, *Energy Environ. Sci.*, **12** (12), 3496-3501 (2019).
8. A. Shyamsunder, L. E. Blanc, A. Assoud, and L. F. Nazar, *ACS Energy Letters*, **4** (9), 2271-2276 (2019).
9. K. V. Nielson, J. Luo, and T. L. Liu, *Batteries & Supercaps*, **3** (8), 766-772 (2020).
10. N. T. Hahn, D. M. Driscoll, Z. Yu, G. E. Sterbinsky, L. Cheng, M. Balasubramanian, and K. R. Zavadil, *ACS Applied Energy Materials*, **3** (9), 8437-8447 (2020).
11. S. H. Lapidus, N. N. Rajput, X. Qu, K. W. Chapman, K. A. Persson, and P. J. Chupas, *Phys. Chem. Chem. Phys.*, **16** (40), 21941-21945 (2014).
12. J. D. Forero-Saboya, E. Marchante, R. B. Araujo, D. Monti, P. Johansson, and A. Ponrouch, *J. Phys. Chem. C*, **123** (49), 29524-29532 (2019).
13. N. T. Hahn, J. Self, T. J. Seguin, D. M. Driscoll, M. A. Rodriguez, M. Balasubramanian, K. A. Persson, and K. R. Zavadil, *J. Mater. Chem. A*, **8** (15), 7235-7244 (2020).
14. A. K. Katz, J. P. Glusker, S. A. Beebe, and C. W. Bock, *J. Am. Chem. Soc.*, **118** (24), 5752-5763 (1996).
15. J. L. Fulton, S. M. Heald, Y. S. Badyal, and J. M. Simonson, *J. Phys. Chem. A*, **107** (23), 4688-4696 (2003).
16. D. S. Tchitchekova, D. Monti, P. Johansson, F. Bardé, A. Randon-Vitanova, M. R. Palacín, and A. Ponrouch, *J. Electrochem. Soc.*, **164** (7), A1384-A1392 (2017).

17. N. N. Rajput, X. Qu, N. Sa, A. K. Burrell, and K. A. Persson, *J. Am. Chem. Soc.,* **137** (9), 3411-3420 (2015).
18. V. Martin-Diaconescu, M. Gennari, B. Gerey, E. Tsui, J. Kanady, R. Tran, J. Pécaut, D. Maganas, V. Krewald, E. Gouré, C. Duboc, J. Yano, T. Agapie, M.-N. Collomb, and S. DeBeer, *Inorg. Chem.,* **54** (4), 1283-1292 (2015).
19. J. L. Fulton, E. J. Bylaska, S. Bogatko, M. Balasubramanian, E. Cauët, G. K. Schenter, and J. H. Weare, *J. Phys. Chem. Lett.,* **3** (18), 2588-2593 (2012).
20. L. X. Dang, G. K. Schenter, V.-A. Glezakou, and J. L. Fulton, *J. Phys. Chem. B,* **110** (47), 23644-23654 (2006).
21. M. D. Baer and C. J. Mundy, *J. Phys. Chem. B,* **120** (8), 1885-1893 (2016).
22. V.-T. Pham and J. L. Fulton, *J. Chem. Phys.,* **138** (4), 044201 (2013).
23. K. Henzler, E. O. Fetisov, M. Galib, M. D. Baer, B. A. Legg, C. Borca, J. M. Xto, S. Pin, J. L. Fulton, G. K. Schenter, N. Govind, J. I. Siepmann, C. J. Mundy, T. Huthwelker, and J. J. De Yoreo, *Science Advances,* **4** (1), eaao6283 (2018).
24. I. Krossing and A. Reisinger, *Coord. Chem. Rev.,* **250** (21), 2721-2744 (2006).
25. B. Ravel and M. Newville, *Journal of Synchrotron Radiation,* **12** (4), 537-541 (2005).
26. M. Newville, *Journal of Physics: Conference Series,* **430** 012007 (2013).
27. J. J. Rehr and R. C. Albers, *Phys. Rev. B,* **41** (12), 8139-8149 (1990).
28. S. I. Zabinsky, J. J. Rehr, A. Ankudinov, R. C. Albers, and M. J. Eller, *Phys. Rev. B,* **52** (4), 2995-3009 (1995).
29. J. Tao, J. P. Perdew, V. N. Staroverov, and G. E. Scuseria, *Phys. Rev. Lett.,* **91** (14), 146401 (2003).
30. F. Weigend and R. Ahlrichs, *Phys. Chem. Chem. Phys.,* **7** (18), 3297-3305 (2005).
31. F. Weigend, *Phys. Chem. Chem. Phys.,* **8** (9), 1057-1065 (2006).
32. F. Neese, *WIREs Computational Molecular Science,* **2** (1), 73-78 (2012).
33. F. Neese, F. Wennmohs, A. Hansen, and U. Becker, *Chem. Phys.,* **356** (1), 98-109 (2009).
34. M. J. Frisch, G. W. Trucks, H. B. Schlegel, G. E. Scuseria, M. A. Robb, J. R. Cheeseman, G. Scalmani, V. Barone, G. A. Petersson, H. Nakatsuji, X. Li, M. Caricato, A. V. Marenich, J. Bloino, B. G. Janesko, R. Gomperts, B. Mennucci, H. P. Hratchian, J. V. Ortiz, A. F. Izmaylov, J. L. Sonnenberg, Williams, F. Ding, F. Lipparini, F. Egidi, J. Goings, B. Peng, A. Petrone, T. Henderson, D. Ranasinghe, V. G. Zakrzewski, J. Gao, N. Rega, G. Zheng, W. Liang, M. Hada, M. Ehara, K. Toyota, R. Fukuda, J. Hasegawa, M. Ishida, T. Nakajima, Y. Honda, O. Kitao, H. Nakai, T. Vreven, K. Throssell, J. A. Montgomery Jr., J. E. Peralta, F. Ogliaro, M. J. Bearpark, J. J. Heyd, E. N. Brothers, K. N. Kudin, V. N. Staroverov, T. A. Keith, R. Kobayashi, J. Normand, K. Raghavachari, A. P. Rendell, J. C. Burant, S. S. Iyengar, J. Tomasi, M. Cossi, J. M. Millam, M. Klene, C. Adamo, R. Cammi, J. W. Ochterski, R. L. Martin, K. Morokuma, O. Farkas, J. B. Foresman, and D. J. Fox, Wallingford, CT, 2016.
35. J.-D. Chai and M. Head-Gordon, *Phys. Chem. Chem. Phys.,* **10** (44), 6615-6620 (2008).
36. Z. Zhao-Karger, M. E. Gil Bardaji, O. Fuhr, and M. Fichtner, *J. Mater. Chem. A,* **5** (22), 10815-10820 (2017).
37. G. A. Giffin, A. Moretti, S. Jeong, and S. Passerini, *J. Phys. Chem. C,* **118** (19), 9966-9973 (2014).
38. R. D. Shannon, *Acta Crystallographica Section A,* **32** (5), 751-767 (1976).
39. T. J. Seguin, N. T. Hahn, K. R. Zavadil, and K. A. Persson, *Frontiers in Chemistry,* **7** (175), (2019).

40. N. N. Rajput, T. J. Seguin, B. M. Wood, X. Qu, and K. A. Persson, *Top. Curr. Chem.*, **376** (3), 19 (2018).
41. K.-C. Lau, T. J. Seguin, E. V. Carino, N. T. Hahn, J. G. Connell, B. J. Ingram, K. A. Persson, K. R. Zavadil, and C. Liao, *J. Electrochem. Soc.*, **166** (8), A1510-A1519 (2019).
42. G. Agarwal, H. A. Doan, and R. S. Assary, *J. Electrochem. Soc.*, **167** (10), 100545 (2020).

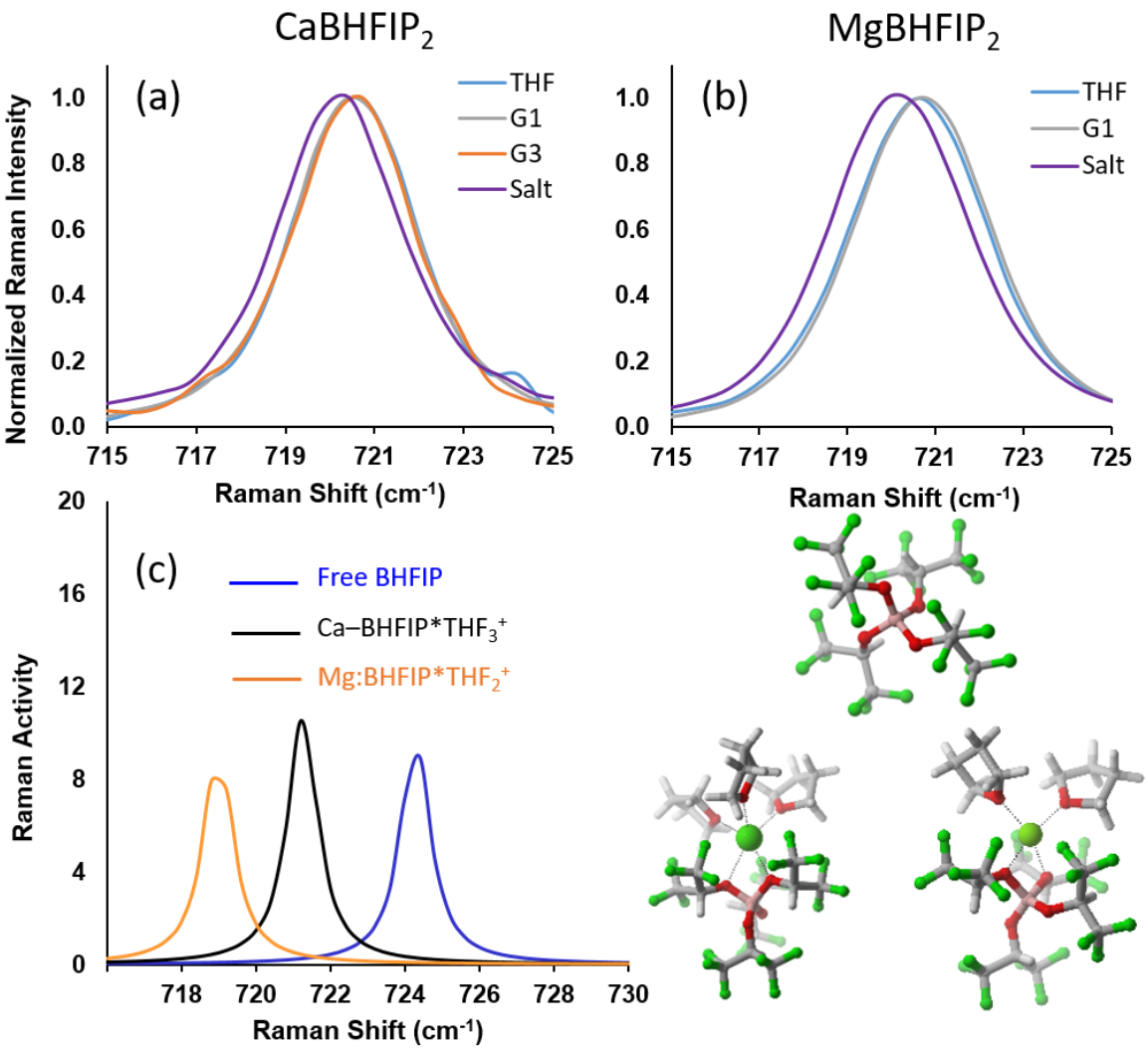

Figure 1. Raman spectra of the ν(C-F) region for 0.5 M $CaBHFIP_2$ (a) and $MgBHFIP_2$ (b) dissolved in ethereal solvents and compared with the corresponding partially de-solvated solid salt containing residual THF. (c) DFT-calculated Raman peak positions based on optimized structures of the free BHFIP anion and the idealized THF-solvated ion pairs of Ca–BHFIP*THF_3^+ and Mg–BHFIP*THF_2^+. The calculated structures of all three species are shown with boron, oxygen, carbon, fluorine and hydrogen shown in pink, red, grey, white and green respectively.

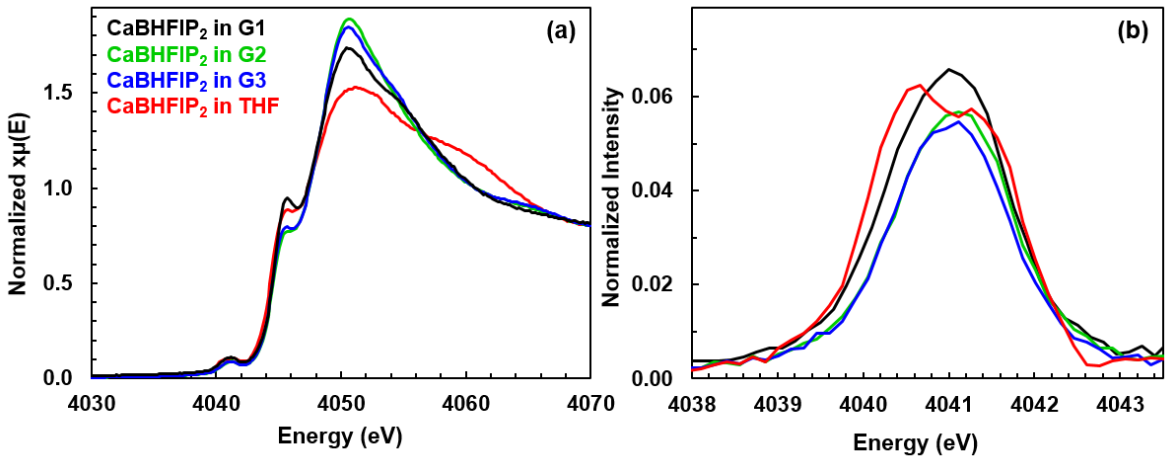

Figure 2. (a) XANES of 0.2 M $CaBHFIP_2$ dissolved in G1, G2, G3 and THF. (b) Background and edge-subtracted pre-edge region for each salt solution.

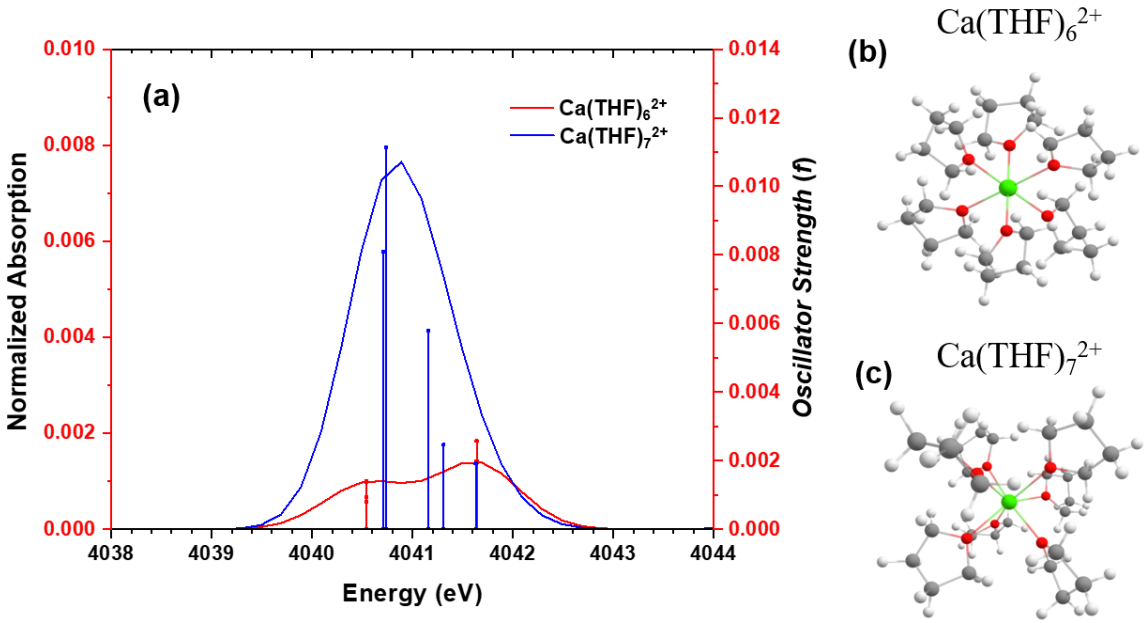

Figure 3. (a) Calculated XAS pre-edge of Ca^{2+} coordinated to THF. In the spectra, the vertical lines represent excitation from Ca 1s to higher orbitals at different energies, with the oscillator strength (*f*) shown on the right y-axis. (b) and (c) are simulated geometries for the 6- and 7-coordinated species.

Table 1. Pre-edge energies and intensities derived from TDDFT simulations

Structure	Symmetry	Calculated				
		Ca-O [Å]	Energy, eV + 50.4	Total Intensity	Dipole Intensity	Quadrupole Intensity
$Ca(THF)_6^{2+}$	Pseudo-octahedral, O_h	2.43 2.42 2.43 2.43 2.42 2.43	4040.54 4040.54 4040.54 4041.64 4041.64	0.0231 0.0155 0.0135 0.0329 0.0428	0.0006 0.0006 0.0005 0.0000 0.0000	0.0220 0.0109 0.0088 0.0275 0.0339
$Ca(THF)_7^{2+}$	C_{2v}/C_{3v}	2.55 2.46 2.58 2.55 2.57 2.47 2.54	4040.71 4040.74 4041.16 4041.31 4041.63	0.1628 0.2243 0.1168 0.0496 0.0386	0.1455 0.2101 0.0881 0.0225 0.0033	0.0167 0.0120 0.0265 0.0219 0.0259

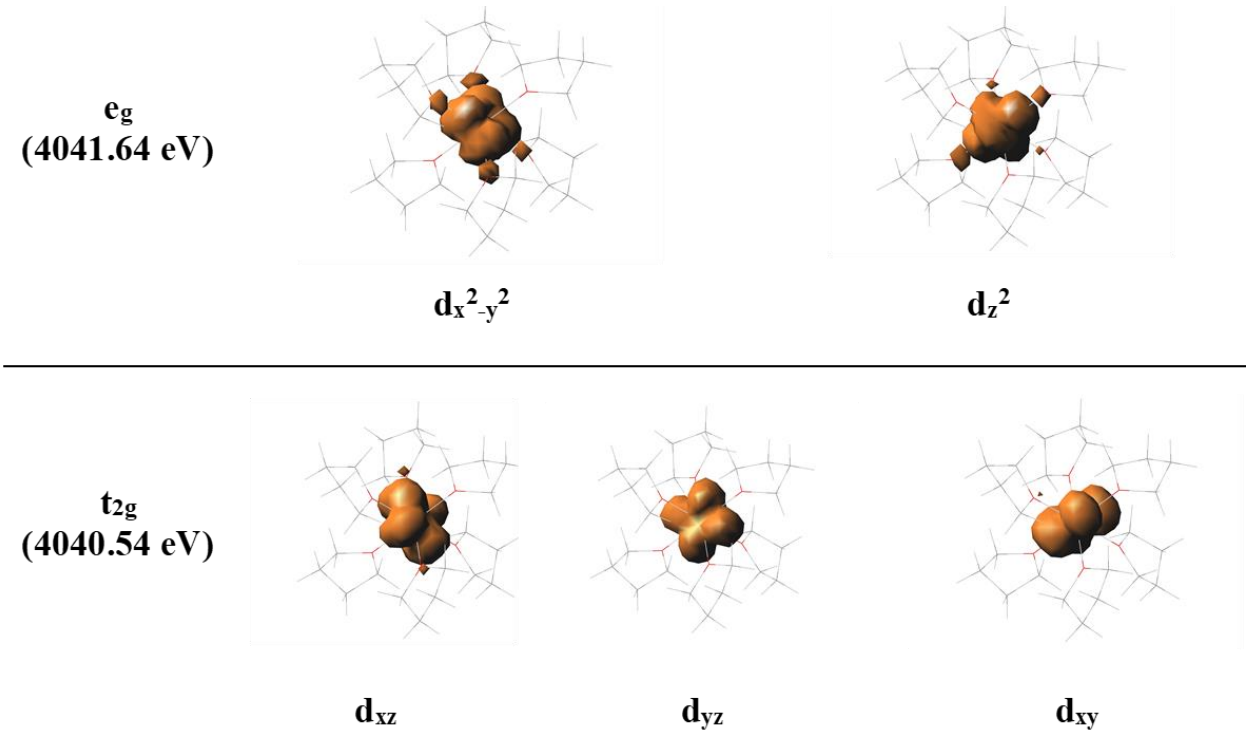

Figure 4. Transition difference density maps for pre-edge peaks in the pseudo octahedral $Ca(THF)_6^{2+}$ model.

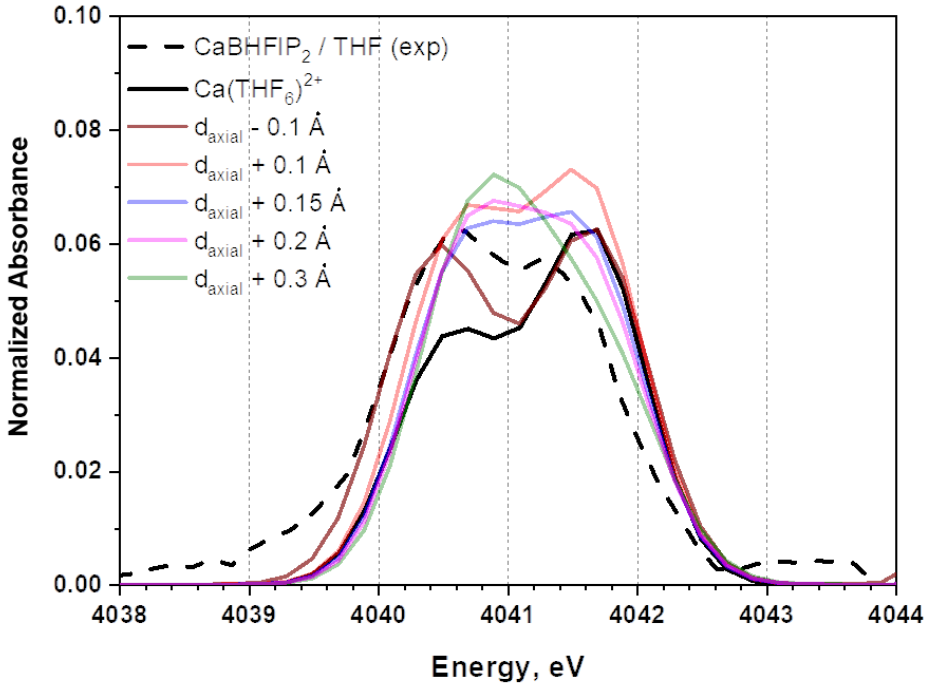

Figure 5. Calculated and experimental XAS showing effect of displacement of Ca-O bond distance on spectral features. Calculated energies were shifted by +50.4 eV and the intensities were multiplied with a factor of 45, to match with the experimental spectra.

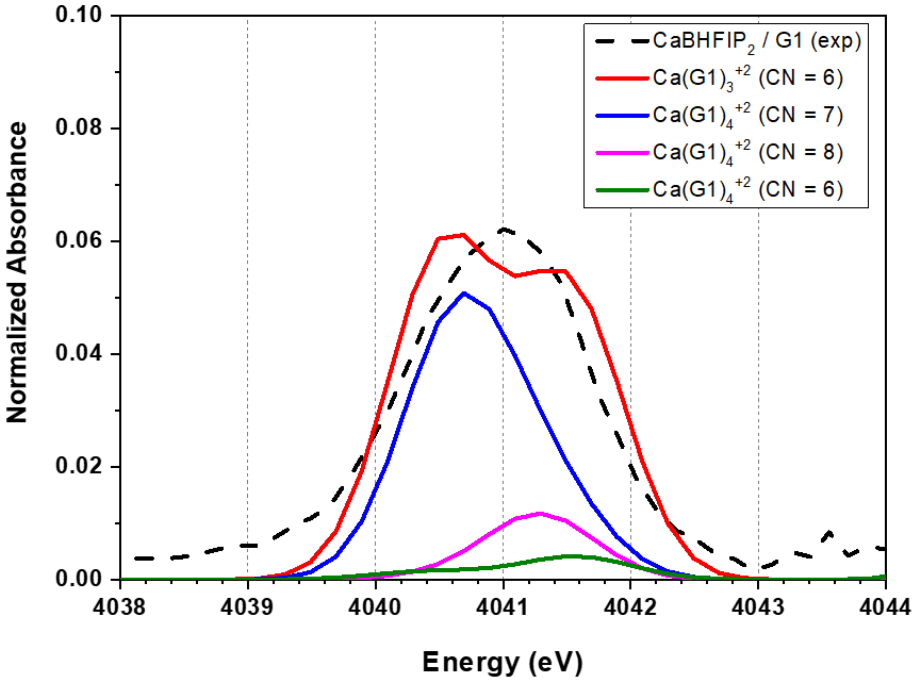

Figure 6. Comparison of TD-DFT (blue, red, and magenta lines) and normalized, edge-subtracted experimental XANES pre-edge regions for the $CaBHFIP_2$/G1 (grey, dashed trace). Calculated energies were shifted by +50.4 eV while the calculated spectra intensities are not adjusted to match with experimental data. The CN value represents the number of Ca–O bonds in the cluster.

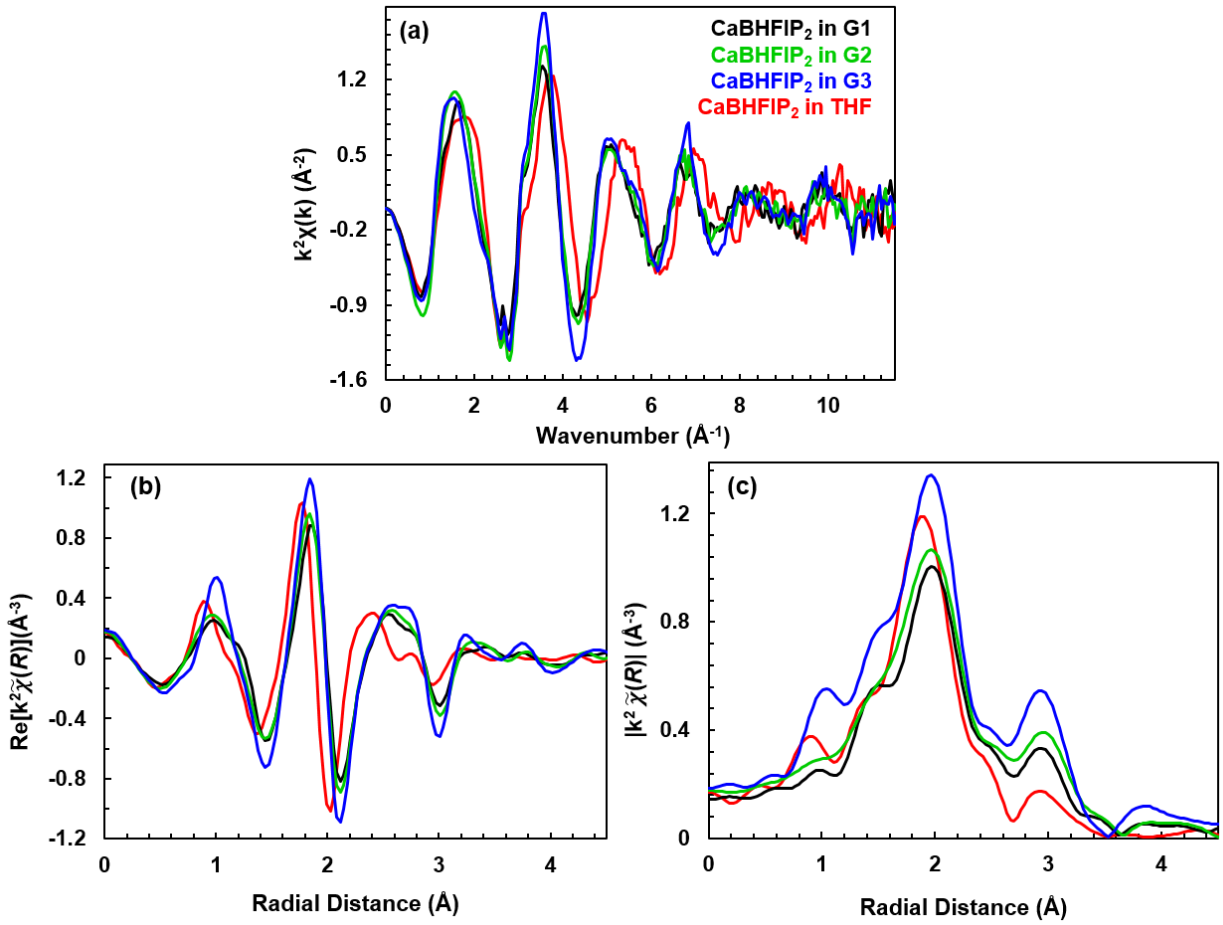

Figure 7. Experimental EXAFS measurements of 0.2 M $CaBHFIP_2$ salts in ethereal solvents. Spectra shown in k^2-weighted $\chi(k)$ (a), real-component of the $[\tilde{X}(R)]$ (b), and $|\tilde{X}(R)|$ (c). Fourier transform were performed over a k-range of 3 – 11 $Å^{-1}$

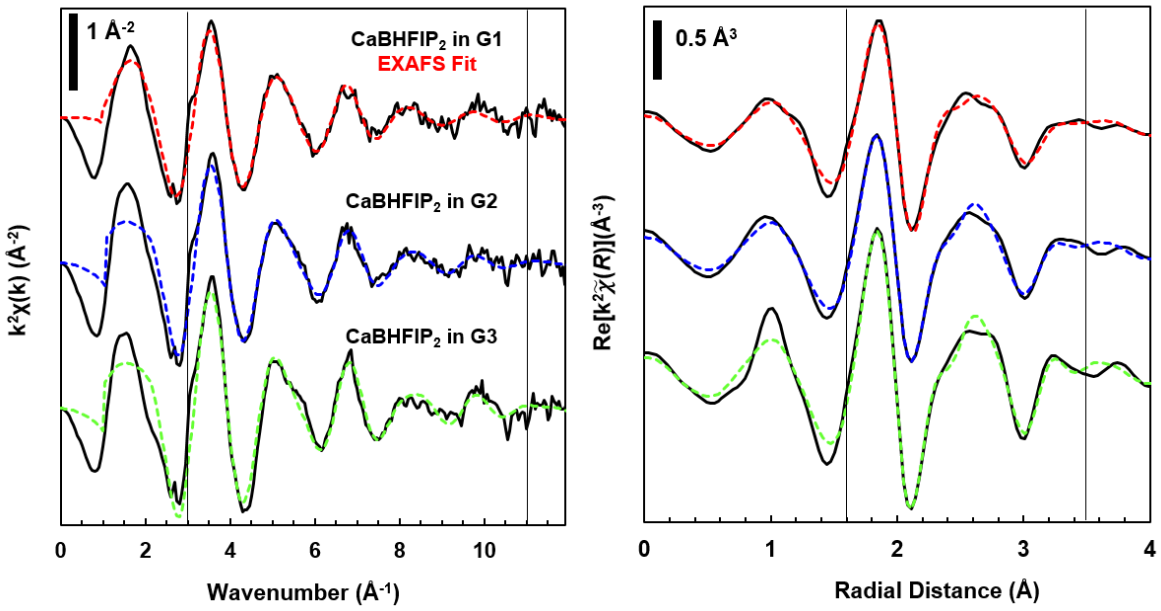

Figure 8. EXAFS analysis of 0.2 M $CaBHFIP_2$ dissolved in G1, G2 and G3 shown in k-space and r-space. Fits represent the optimization of a sum of individual photoelectron scattering paths.

Table 2. EXAFS parameters derived from fitting the 0.2 M $CaBHFIP_2$ in glyme series. Each model assumes that each solvent coordinates as a multidentate ligand.

	Solvent		
	G1	G2	G3
CN: Ca–O	6.6 ± 0.8	7.0 ± 0.7	7.8 ± 0.9
R: Ca–O (Å)	2.48 ± 0.01	2.45 ± 0.01	2.45 ± 0.01
$\sigma^2_{Ca\text{-}O}$ ($Å^2$)	0.011 ± 0.002	0.011 ± 0.002	0.009 ± 0.002
$\sigma^2_{Ca\text{-}C}$ ($Å^2$)	0.020 ± 0.006	0.014 ± 0.004	0.009 ± 0.003
k-window ($Å^{-1}$)	3 – 11		
r-window (Å)	1.6 – 3.5		